

WEAK HARD X-RAY EMISSION FROM BROAD ABSORPTION LINE QUASARS: EVIDENCE FOR INTRINSIC X-RAY WEAKNESS

B. LUO,^{1,2} W. N. BRANDT,^{1,2} D. M. ALEXANDER,³ D. STERN,⁴ S. H. TENG,⁵ P. ARÉVALO,^{6,7} F. E. BAUER,^{6,8,9} S. E. BOGGS,¹⁰ F. E. CHRISTENSEN,¹¹ A. COMASTRI,¹² W. W. CRAIG,^{13,10} D. FARRAH,¹⁴ P. GANDHI,³ C. J. HAILEY,¹⁵ F. A. HARRISON,¹⁶ M. KOSS,¹⁷ P. OGLE,¹⁸ S. PUC CETTI,^{19,20} C. SAEZ,²¹ A. E. SCOTT,^{1,2} D. J. WALTON,¹⁶ & W. W. ZHANG²²

Draft version August 19, 2014

ABSTRACT

We report *NuSTAR* observations of a sample of six X-ray weak broad absorption line (BAL) quasars. These targets, at $z = 0.148\text{--}1.223$, are among the optically brightest and most luminous BAL quasars known at $z < 1.3$. However, their rest-frame ≈ 2 keV luminosities are 14 to > 330 times weaker than expected for typical quasars. Our results from a pilot *NuSTAR* study of two low-redshift BAL quasars, a *Chandra* stacking analysis of a sample of high-redshift BAL quasars, and a *NuSTAR* spectral analysis of the local BAL quasar Mrk 231 have already suggested the existence of intrinsically X-ray weak BAL quasars, i.e., quasars not emitting X-rays at the level expected from their optical/UV emission. The aim of the current program is to extend the search for such extraordinary objects. Three of the six new targets are weakly detected by *NuSTAR* with $\lesssim 45$ counts in the 3–24 keV band, and the other three are not detected. The hard X-ray (8–24 keV) weakness observed by *NuSTAR* requires Compton-thick absorption if these objects have nominal underlying X-ray emission. However, a soft stacked effective photon index ($\Gamma_{\text{eff}} \approx 1.8$) for this sample disfavors Compton-thick absorption in general. The uniform hard X-ray weakness observed by *NuSTAR* for this and the pilot samples selected with < 10 keV weakness also suggests that the X-ray weakness is intrinsic in at least some of the targets. We conclude that the *NuSTAR* observations have likely discovered a significant population ($\gtrsim 33\%$) of intrinsically X-ray weak objects among the BAL quasars with significantly weak < 10 keV emission. We suggest that intrinsically X-ray weak quasars might be preferentially observed as BAL quasars.

Subject headings: accretion, accretion disks – galaxies: active – galaxies: nuclei – quasars: absorption lines – quasars: emission lines – X-rays: galaxies

¹ Department of Astronomy & Astrophysics, 525 Davey Lab, The Pennsylvania State University, University Park, PA 16802, USA

² Institute for Gravitation and the Cosmos, The Pennsylvania State University, University Park, PA 16802, USA

³ Department of Physics, Durham University, South Road, Durham DH1 3LE, UK

⁴ Jet Propulsion Laboratory, California Institute of Technology, Pasadena, CA 91109, USA

⁵ Observational Cosmology Laboratory, NASA Goddard Space Flight Center, Greenbelt, MD 20771, USA

⁶ Instituto de Astrofísica, Facultad de Física, Pontificia Universidad Católica de Chile, 306, Santiago 22, Chile

⁷ Instituto de Física y Astronomía, Facultad de Ciencias, Universidad de Valparaíso, Gran Bretaña 1111, Playa Ancha, Valparaíso, Chile

⁸ Millennium Institute of Astrophysics, Vicuña Mackenna 4860, 7820436 Macul, Santiago, Chile

⁹ Space Science Institute, 4750 Walnut Street, Suite 205, Boulder, CO 80301, USA

¹⁰ Space Sciences Laboratory, University of California, Berkeley, CA 94720, USA

¹¹ DTU Space - National Space Institute, Technical University of Denmark, Elektrovej 327, 2800 Lyngby, Denmark

¹² INAF—Osservatorio Astronomico di Bologna, Via Ranzani 1, Bologna, Italy

¹³ Lawrence Livermore National Laboratory, Livermore, CA 94550, USA

¹⁴ Department of Physics, Virginia Tech, Blacksburg, VA 24061, USA

¹⁵ Columbia Astrophysics Laboratory, Columbia University, New York, NY 10027, USA

¹⁶ Cahill Center for Astronomy and Astrophysics, California Institute of Technology, Pasadena, CA 91125, USA

¹⁷ Institute for Astronomy, Department of Physics, ETH Zurich, Wolfgang-Pauli-Strasse 27, CH-8093 Zurich, Switzerland

¹⁸ IPAC, California Institute of Technology, Mail Code 220-6, Pasadena, CA 91125, USA

¹⁹ ASDC—ASI, Via del Politecnico, 00133 Roma, Italy

²⁰ INAF—Osservatorio Astronomico di Roma, via Frascati 33, 00040

Monte Porzio Catone (RM), Italy

²¹ Department of Astronomy, University of Maryland, College Park, MD 20742, USA

²² NASA Goddard Space Flight Center, Greenbelt, MD 20771, USA

1. INTRODUCTION

X-ray emission is considered to be ubiquitous from active galactic nuclei (AGNs), and it is believed to originate from a hot “corona” surrounding the inner accretion disk via Comptonization of disk optical/UV/EUV photons (e.g., Haardt & Maraschi 1991). X-ray emission may be enhanced in radio-loud AGNs due to the contribution from jets, and the X-ray weakness observed in some AGNs is generally attributed to absorption. After excluding radio-loud AGNs and potentially X-ray absorbed AGNs, a highly significant correlation between the AGN UV luminosity (2500 Å monochromatic luminosity, $L_{2500 \text{ Å}}$) and the X-ray-to-optical power-law slope parameter (α_{OX})²³ has been established across ≈ 5 orders of magnitude in UV luminosity (e.g., Steffen et al. 2006; Just et al. 2007; Lusso et al. 2010). This relation highlights apparently uniform physical mechanisms at work at the heart of the AGN engine.

One might naturally wonder whether there are AGNs that are intrinsically X-ray weak, producing much less X-ray emission than expected from the $\alpha_{\text{OX}}-L_{2500 \text{ Å}}$ relation. One such example is PHL 1811, a very bright quasar at $z = 0.19$ with a B -band magnitude of 13.9 that has been studied extensively (e.g., Leighly et al. 2007a,b). It is believed to be intrinsically X-ray weak by a factor of ≈ 30 –100. A small sample of Sloan Digital Sky Survey (SDSS; York et al. 2000) quasars with similar emission-line properties, termed “PHL 1811 analogs”, has also been observed to be X-ray weak (Wu et al. 2011), although the nature of their X-ray weakness (intrinsic X-ray weakness or absorption) is uncertain. The fraction of PHL 1811 analogs in the radio-quiet quasar population is small, $\lesssim 1.2\%$. As a first attempt to constrain the fraction of intrinsically X-ray weak AGNs systematically, Gibson et al. (2008) searched for such objects among optically selected SDSS quasars, again excluding radio-loud AGNs and potentially X-ray absorbed systems. Their conclusion was that such AGNs are rare; e.g., the fraction is $\lesssim 2\%$ for AGNs that are intrinsically X-ray weak by a factor of 10 or more. Discovery of intrinsically X-ray weak AGNs challenges the idea of a universal X-ray emission mechanism, and studies of such objects should provide insights into the nature of the corona.

There is one significant population of AGNs that belongs to the category of potentially X-ray absorbed AGNs which has been excluded in previous searches for intrinsically X-ray weak AGNs, and this is broad absorption line (BAL) quasars. BAL quasars comprise $\approx 15\%$ of optically selected quasars (e.g., Hewett & Foltz 2003; Trump et al. 2006; Gibson et al. 2009; Allen et al. 2011), and observationally they are in general X-ray weak, often due to absorption (e.g., Gallagher et al. 2002a, 2006; Fan et al. 2009; Gibson et al. 2009). In the accretion-disk wind model (see Figure 1 of Luo et al. 2013, hereafter L13), where a radiatively driven wind is launched from the accretion disk at $\approx 10^{16}$ – 10^{17} cm (e.g., Murray et al. 1995; Proga et al. 2000), BALs are observed when the inclination angle is large and the line of sight passes through the outflowing wind. In this model, suppression of the nuclear X-ray emission is required to prevent the wind from being overionized. Some “shielding” material, e.g., the shielding gas as shown in Figure 1 of L13, is usually invoked to provide X-ray absorption in BAL quasars, which is consistent

with the absorption typically observed. However, if a BAL quasar were intrinsically X-ray weak, the wind could also be launched successfully with little or no shielding.

Indeed, there are some BAL quasars with significant X-ray weakness that cannot be accounted for by the apparent X-ray absorption determined using < 10 keV *Chandra* or *XMM-Newton* data (e.g., Sabra & Hamann 2001; L13). These are candidates for intrinsically X-ray weak AGNs. It is also possible that they are intrinsically X-ray normal but are heavily obscured ($N_{\text{H}} \gtrsim 5 \times 10^{23} \text{ cm}^{-2}$) or even Compton-thick ($N_{\text{H}} \geq 1.5 \times 10^{24} \text{ cm}^{-2}$), so that the observed < 10 keV spectra are dominated by a Compton-reflected component. To distinguish between the intrinsic X-ray weakness and heavy absorption scenarios, observations of highly penetrating X-rays in the > 10 keV rest-frame band are required.

In L13, we presented *NuSTAR* (Harrison et al. 2013) 3–79 keV observations of a pilot sample of two such BAL quasars, PG 1004+130 ($z = 0.241$) and PG 1700+518 ($z = 0.292$). Both objects are surprisingly X-ray weak in the *NuSTAR* band, suggesting either intrinsic X-ray weakness or highly Compton-thick absorption ($N_{\text{H}} \approx 7 \times 10^{24} \text{ cm}^{-2}$). Additionally, a *Chandra* stacking analysis in L13 with the Large Bright Quasar Survey (LBQS) BAL-quasar sample at high redshift (where *Chandra* probes the rest-frame ≈ 1.5 –24 keV band) revealed an effective power-law photon index of $\Gamma_{\text{eff}} = 1.6^{+0.6}_{-0.5}$. This effective photon index is fairly soft/steep for a spectrum expected to be absorbed, and it argues against Compton-thick absorption in general, which would usually result in a hard/flat ($\Gamma_{\text{eff}} \approx 0.5$ with a range of ≈ 0 –1) spectrum (e.g., George & Fabian 1991; Comastri et al. 2011; Gandhi et al. 2014; Rovilos et al. 2014). This result suggests a significant fraction (≈ 17 –40%) of intrinsically X-ray weak BAL quasars in this sample. Subsequently, *NuSTAR* observations of the nearest BAL quasar, Mrk 231, obtained hard X-ray spectra with sufficient photon statistics for spectral fitting. A joint *Chandra* and *NuSTAR* spectral analysis, though challenging due to the substantial spectral complexity present, suggests Compton-thin absorption ($N_{\text{H}} \approx 1.2 \times 10^{23} \text{ cm}^{-2}$), making Mrk 231 intrinsically X-ray weak by a factor of ≈ 10 (Teng et al. 2014). These *NuSTAR* and *Chandra* results provide the first clear evidence for the existence of intrinsically X-ray weak BAL quasars.

As an extension of the L13 pilot program, we obtained 20–35 ks *NuSTAR* observations of an additional six BAL quasars that show significant X-ray weakness in the < 10 keV band. The aim is to evaluate whether they show similar hard X-ray weakness to the pilot sample. The nature of the X-ray weakness, whether intrinsic or due to Compton-thick absorption, can be assessed via stacking analyses or statistical arguments for the full sample of eight BAL quasars, including the two L13 objects. We describe the sample selection and *NuSTAR* data analysis in Sections 2 and 3. The stacking analyses and column-density constraints are presented in Section 4. We discuss the possibility of intrinsic X-ray weakness for our sample in Section 5, and we summarize in Section 6. Throughout this paper, we use J2000.0 coordinates and a cosmology with $H_0 = 70.4 \text{ km s}^{-1} \text{ Mpc}^{-1}$, $\Omega_{\text{M}} = 0.272$, and $\Omega_{\Lambda} = 0.728$ (e.g., Komatsu et al. 2011). Full names of the targets are listed in the tables while abbreviated names are used in the text. We quote uncertainties at a 1σ confidence level and upper and lower limits at a 90% confidence level, unless otherwise stated.

²³ α_{OX} is defined as $\alpha_{\text{OX}} = -0.3838 \log(f_{2500 \text{ Å}}/f_{2 \text{ keV}})$, where $f_{2500 \text{ Å}}$ and $f_{2 \text{ keV}}$ are the rest-frame 2500 Å and 2 keV flux densities.

2. SAMPLE SELECTION

We selected BAL-quasar targets based on the following four criteria:

1. The targets are bona-fide BAL quasars with C IV $\lambda 1549$ absorption-trough widths $> 2000 \text{ km s}^{-1}$.
2. The targets are optically bright ($m_B \lesssim 16$) so that we would expect a significant number of hard X-ray photons detected with *NuSTAR* provided they have nominal underlying X-ray emission as expected from the $\alpha_{\text{OX}}-L_{2500 \text{ \AA}}$ relation and they are not Compton-thick.
3. The targets are significantly X-ray weak in the $\lesssim 10 \text{ keV}$ band with X-ray weakness that cannot be accounted for by any apparent X-ray absorption determined using *Chandra* or *XMM-Newton* data.²⁴ Therefore, they are either intrinsically X-ray weak or heavily obscured. *NuSTAR* $> 10 \text{ keV}$ observations will help to discriminate between these two scenarios.
4. The targets are radio quiet (radio-loudness parameter $R < 10$)²⁵ so that their X-ray emission is not contaminated by any jet-linked emission.

We searched for such targets in the $z < 0.5$ Palomar-Green (PG) quasar sample (Schmidt & Green 1983) and in literature reports of BAL quasars with significant X-ray weakness. The six targets are listed in Table 1, of which PG 0043 and PG 1001 are among the $z < 0.5$ PG quasar sample, while IRAS 07598 (e.g., Gallagher et al. 1999; Imanishi & Terashima 2004; Saez et al. 2012), PG 0946 (e.g., Mathur et al. 2000; Saez et al. 2012), PG 1254 (e.g., Sabra & Hamann 2001), and IRAS 14026 (e.g., Saez et al. 2012) are from the literature. These BAL quasar targets have *B*-band magnitudes of ≈ 15 -16, and they are among the optically brightest and most luminous BAL quasars known at $z < 1.3$ (Figure 1). The more luminous PG 0946 and PG 1254 are also representative counterparts of the luminous BAL quasars typically studied at $z \approx 2$ -3 (e.g., Gibson et al. 2009).

There are five BAL quasars among the $z < 0.5$ PG quasar sample (see Footnote 4 of Brandt et al. 2000), four of which have now been included in our *NuSTAR* BAL quasar program (PG 0043 and PG 1001 here and PG 1004 and PG 1700 in L13).²⁶ Therefore, we are sampling a significant fraction of the most luminous BAL quasars at low redshifts. The sample completeness among the general population of BAL quasars is not clear as there have been no systematic identifications of BAL quasars at low redshifts, which usually require *Hubble Space Telescope* spectra covering the key C IV $\lambda 1549$ transition.

²⁴ We require a factor of $\gtrsim 10$ times X-ray weakness at $\approx 2 \text{ keV}$ by comparing the measured α_{OX} parameter to the one expected from the $\alpha_{\text{OX}}-L_{2500 \text{ \AA}}$ relation, and also a factor of $\gtrsim 2$ times X-ray weakness in the observed 2-8 keV band by measuring the $\alpha_{\text{OX,corr}}$ parameter (see Section 1.1 of L13 for discussion of $\alpha_{\text{OX,corr}}$). In fact, the objects ultimately selected for our sample generally exceed these requirements by a substantial margin (see below).

²⁵ $R = f_5 \text{ GHz} / f_{4400 \text{ \AA}}$ (the ratio between the 5 GHz and 4400 \AA flux densities in the rest frame; e.g., Kellermann et al. 1989). We obtained radio flux information from the Faint Images of the Radio Sky at Twenty-Centimeters (FIRST) survey (Becker et al. 1995) or the NRAO VLA Sky Survey (NVSS; Condon et al. 1998).

²⁶ The other BAL quasar is PG 2112+059, the X-ray weakness of which can be explained by moderate absorption (e.g., Gallagher et al. 2001, 2004).

All six targets have archival *Chandra* and/or *XMM-Newton* observations. The X-ray observations of IRAS 07598, PG 0946, PG 1001, and IRAS 14026 are summarized in Saez et al. (2012) and references therein. PG 1254 has a 36 ks *Chandra* observation that was reported in Sabra & Hamann (2001). PG 0043 has two $\approx 30 \text{ ks}$ *XMM-Newton* observations. The source was not detected in the first observation and data for the second observation are not publicly available yet. We reprocessed the public *Chandra* and *XMM-Newton* data and obtained the α_{OX} parameters for the targets, with $f_2 \text{ keV}$ derived from the observed 0.5-2 keV flux and $f_{2500 \text{ \AA}}$ derived by interpolating the optical-UV photometric data (see Section 5.1 below). The α_{OX} constraints for the targets are shown in Figure 2, which indicate that their rest-frame $\approx 2 \text{ keV}$ luminosities are 14 to > 330 times weaker than expected from the Steffen et al. (2006) $\alpha_{\text{OX}}-L_{2500 \text{ \AA}}$ relation. These α_{OX} values have not been corrected for any intrinsic optical/UV reddening, which would render the values even more negative. Note that the spread of the Steffen et al. (2006) data points constrains the expected amount of quasar variability (e.g., Gibson & Brandt 2012), and after accounting for the measured flux variability of our targets (see Section 3 below), they are still significantly X-ray weak. Also evident in Figure 2 is the significant $\approx 2 \text{ keV}$ weakness of PG 1004, PG 1700, and Mrk 231 (L13; Teng et al. 2014). In addition, we verified that these targets are still X-ray weak (by factors of ≈ 2 to > 220) in a somewhat harder band by measuring $\alpha_{\text{OX,corr}}$ with the observed 2-8 keV flux assuming a $\Gamma = 1.8$ power-law spectrum (see Section 1.1 of L13). Given the significant X-ray weakness of these six targets, they could be either heavily obscured or intrinsically X-ray weak.

There have been no previous tight constraints on the $> 10 \text{ keV}$ emission of these objects. They are not detected in the 70 month *Swift*-BAT 14-195 keV all-sky survey (Baumgartner et al. 2013), the sensitivity of which falls short by an order of magnitude even if they have nominal hard X-ray emission. With the much higher sensitivity of *NuSTAR*, the hard X-ray emission of these objects can be sensitively constrained with relatively short exposure times. Assuming that the targets are intrinsically X-ray normal with an underlying 2 keV luminosity determined by the $\alpha_{\text{OX}}-L_{2500 \text{ \AA}}$ relation, we can estimate the *NuSTAR* counts yield following the approach in Section 4.1.1 of L13 using the MYTORUS model (Murphy & Yaqoob 2009). Provided that the sources are Compton-thin ($N_{\text{H}} < 1.5 \times 10^{24} \text{ cm}^{-2}$), we would expect significant detections of PG 0043, IRAS 07598, PG 1001, and IRAS 14026 in the 8-24 keV band (more than 80-260 counts where these values are derived for $N_{\text{H}} = 1.5 \times 10^{24} \text{ cm}^{-2}$) with 20 ks *NuSTAR* observations. Longer exposures are required for the more distant targets PG 0946 (35 ks) and PG 1254 (30 ks) for a 8-24 keV detection with more than 30 counts. Fewer counts are expected, of course, if the targets are either intrinsically X-ray weak or have Compton-thick column densities substantially exceeding $1.5 \times 10^{24} \text{ cm}^{-2}$.

3. *NuSTAR* OBSERVATIONS AND DATA ANALYSIS

The details of the *NuSTAR* observations are listed in Table 1. We processed the level 1 data using the *NuSTAR* Data Analysis Software (NuSTARDAS) v.1.2.0 with *NuSTAR* CALDB 20131007, and produced cleaned calibrated event files (level 2 data) using the NUPipeline script for both focal plane modules (FPMs, including FPMA and FPMB; Harrison et al. 2013). For each target in each FPM, we created

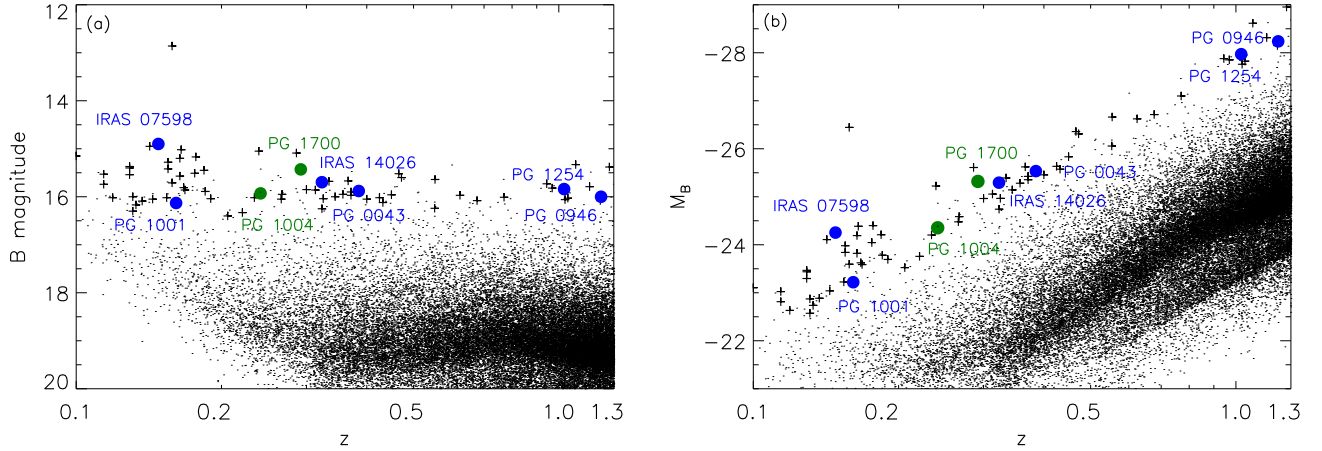


Figure 1. Redshift vs. (a) apparent and (b) absolute B -band magnitudes for our sample objects (blue filled circles). The green filled circles represent the two targets in L13. The plus signs are the bright PG quasars from Schmidt & Green (1983); the brightest object is PG 1226+023 (3C 273). The underlying black dots are objects from the SDSS DR7 quasar catalog (Schneider et al. 2010). The B -band magnitudes of the SDSS quasars were converted from the g -band magnitudes, assuming an optical power-law slope of $\alpha_0 = -0.5$ ($f_\nu \propto \nu^\alpha$; e.g., Vanden Berk et al. 2001). The K -corrections were performed assuming the same optical power-law slope. Our targets are among the optically brightest and most luminous BAL quasars known at $z < 1.3$.

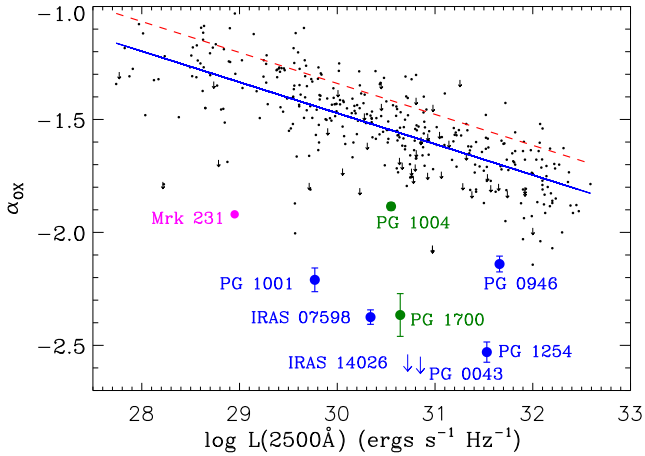


Figure 2. X-ray-to-optical power-law slope (α_{OX}) vs. 2500 Å monochromatic luminosity (not corrected for intrinsic reddening) for the six targeted X-ray weak BAL quasars (blue data points). Also shown are the two objects in the pilot sample (green; L13) and Mrk 231 (magenta; Teng et al. 2014). The small black dots and downward arrows (upper limits) are from the sample of Steffen et al. (2006) with the solid blue line showing the α_{OX} - L_{2500} relation. The dashed red line represents the Steffen et al. (2006) relation modified with the excess X-ray luminosity expected for the radio loudness of PG 1004+130 (Miller et al. 2011). All these BAL quasars are significantly X-ray weak at rest-frame ≈ 2 keV.

X-ray images in four bands: 3–24 keV, 3–8 keV, 8–24 keV, and 24–79 keV using the *Chandra* Interactive Analysis of Observations (CIAO)²⁷ v4.5 tool DMCPY. These bands are being adopted as standard photometric bands in current *NuSTAR* studies (e.g., Alexander et al. 2013; Lansbury et al. 2014), but they are slightly different from those used in the early L13 pilot study (e.g., 4–20 keV, 4–10 keV, and 10–20 keV bands). We have verified that alternative choices of photometric bands yield consistent results.

We searched for sources in each of the images using the CIAO tool WAVDETECT (Freeman et al. 2002) with a false-positive probability threshold of 10^{-5} and wavelet scales of 2, 2.83, 4, 5.66, 8, 11.31, and 16 pixels (the pixel size is $2.46''$). PG 0946, PG 1001, and PG 1254 are detected in at least

one band in each FPM. The minimum positional offsets (Table 1) between the optical and 3–24 keV positions are within expectations for faint sources. The chance of getting any spurious detections by WAVDETECT at these known source positions is negligible. The other three targets, PG 0043, IRAS 07598, and IRAS 14026, are not detected; we also verified the non-detections via visual inspection of the smoothed images. None of the targets is detected in the 24–79 keV band, and the constraints from the non-detections in this band are not as tight as those in the other bands. Stacking in this band does not yield any useful constraints either. Therefore, we do not include the 24–79 keV band in the following discussion.

We performed aperture photometry for each target in the three standard bands above. Total (source plus background) counts were extracted within a $35''$ -radius circular aperture, centered on the 3–24 keV position (for detected targets) or optical position (for undetected targets). This aperture approximates the 63.9% encircled-energy fraction contour of the point spread function, and we have verified that different choices of the source-extraction region yield consistent results. Background counts were extracted from a simulated background map created using the NUSKYBGD script (Wik et al. 2014); these are consistent with those estimated from annular or circular off-source regions. We followed the binomial no-source probability (P_B) approach in L13 to determine the source detection significance in each *NuSTAR* band. If the P_B value is smaller than 0.01 ($\approx 2.6\sigma$), we considered the source detected and calculated the 1σ errors on the net counts (Gehrels 1986). If the P_B value is larger than 0.01, we considered the source undetected and derived an upper limit on the source counts using the Bayesian approach of Kraft et al. (1991). The aperture-corrected source counts and upper limits for our targets are listed in Table 2. Measurements for FPMA and FPMB are consistent within the uncertainties. In the 8–24 keV band, none of the targets is detected except PG 0946 in FPMA with a 23-count detection; the source counts are below our expectations for the Compton-thin scenario (Section 2), and thus all targets are hard X-ray weak, similar to the pilot sample in L13.

Since a relatively large aperture with a $35''$ radius was used in photometry extraction, we investigated whether there are

²⁷ See <http://cxc.harvard.edu/ciao/> for details on CIAO.

any contaminating sources nearby. We inspected the *Chandra* or *XMM-Newton* images for our targets, and confirmed that there is no neighboring source within $50''$ of the targets except PG 0043. There is one source $25''$ away from PG 0043 that was reported in Ballo et al. (2008). The *XMM-Newton* data show a soft spectrum ($\Gamma = 1.86$) with a 2–10 keV flux of 1.8×10^{-14} erg cm $^{-2}$ s $^{-1}$. We estimated that the contamination from this source in our aperture is negligible (≈ 0.8 counts in the 3–8 keV band and ≈ 0.5 counts in the 8–24 keV band). This source should not affect our stacking results below (Section 4.1) either.

Following L13, we derived a 3–24 keV effective power-law photon index (Γ_{eff}) from the band ratio between the 8–24 keV and 3–8 keV bands, calibrated using the *NuSTAR* spectral response files extracted at the source location and assuming a power-law spectrum with the Galactic absorption column density (Dickey & Lockman 1990). The uncertainties of (or limits on) the band ratios (and subsequently Γ_{eff}) were derived using the Bayesian code BEHR (Park et al. 2006). For sources undetected in both the 8–24 keV and 3–8 keV bands, $\Gamma_{\text{eff}} = 1.8$ was adopted. The Γ_{eff} values are listed in Table 2, which do not individually provide tight constraints on whether the sources have hard (indicative of absorption) or soft spectra, due to the non-detections or large uncertainties. The source fluxes and luminosities, listed in Table 2, were converted from the count rates and Γ_{eff} , calibrated with the spectral response files.

We compared the *NuSTAR* 3–8 keV flux measurements to previous *Chandra* and *XMM-Newton* data. Long-term flux variability is observed in the three detected targets. The 3–8 keV flux of PG 0946 has dropped by a factor of 5.4 ± 2.8 between the 2010 *Chandra* observation (Saez et al. 2012) and the *NuSTAR* observation. The *NuSTAR* flux of PG 1001 is consistent with that measured in the 2003 *XMM-Newton* observation, and it is 4.9 ± 2.9 times higher than the flux in the 2010 *Chandra* observation (Saez et al. 2012). PG 1254 is 2.7 ± 1.4 times brighter in the *NuSTAR* observation compared to the 2000 *Chandra* observation (Sabra & Hamann 2001). We note that after accounting for their flux increases, PG 1001 and PG 1254 are still 21 and 58 times X-ray weak at ≈ 2 keV (e.g., in Figure 2), respectively. Similar flux variability has also been noted in PG 1004 in the pilot sample (Miller et al. 2006; L13) and several other BAL quasars (e.g., Gallagher et al. 2004; Saez et al. 2012). For the other three undetected targets, the flux upper limits on IRAS 07598 and IRAS 14026 are consistent with previous *Chandra* and/or *XMM-Newton* flux measurements, and PG 0043 is not detected by *XMM-Newton* either. For IRAS 07598 and IRAS 14026, combining the 3–8 keV fluxes from *Chandra* or *XMM-Newton* and the 8–24 keV flux upper limits from *NuSTAR* does not provide useful constraints on Γ_{eff} . It is not useful to combine the lower energy data with the *NuSTAR* data for the three detected targets due to the observed variability.

4. RESULTS

4.1. Stacking and Joint Spectral Analyses

Since our targets are only weakly detected or undetected by *NuSTAR*, we cannot study the nature of their hard X-ray weakness via individual spectral analysis. Instead, we performed stacking and joint spectral analyses to probe the average spectral properties of the sample. First, we stacked the FPMA and FPMB data for each object individually. The three undetected

targets are still not detected. PG 0946 and PG 1254 are detected in the 8–24 keV band, allowing better constraints on their effective photon indices. For PG 0946, we obtained a Γ_{eff} of $1.2^{+0.7}_{-0.6}$, consistent with its FPMA measurement. For PG 1254, Γ_{eff} is $1.5^{+0.8}_{-0.6}$.

Stacking of the full sample of six objects in both FPMA and FPMB yields significant detections in both the 3–8 keV and 8–24 keV bands, with $164.5^{+31.0}_{-29.4}$ and $102.3^{+29.9}_{-28.3}$ counts, respectively. The band ratio to Γ_{eff} conversion factors vary slightly between different sources, and thus we adopted the average value to convert the 8–24 keV to 3–8 keV band ratio of the stacked source to an effective photon index, which is $\Gamma_{\text{eff}} = 1.8^{+0.5}_{-0.4}$. This Γ_{eff} represents the weighted average of the individual effective photon indices; the weight varies (by factors of a few) between sources due to their different fluxes, exposure times, and rest-frame bands probed. For the subsample of the three detected targets, the stacked counts in the 3–8 keV and 8–24 keV bands are $115.7^{+23.5}_{-21.8}$ and $92.0^{+23.7}_{-22.1}$, respectively, and the effective photon index is $\Gamma_{\text{eff}} = 1.5^{+0.4}_{-0.4}$; for the undetected subsample, the stacked source is only weakly detected in the 3–8 keV band, and the stacked counts in the 3–8 keV and 8–24 keV bands are $48.8^{+21.3}_{-19.7}$ and < 38.1 , respectively, with $\Gamma_{\text{eff}} > 0.8$. Given the Γ_{eff} values for the stacking of the full sample and the detected subsample, the stacked source for the undetected subsample is likely soft, e.g., the lower limit on Γ_{eff} at a less conservative 1σ confidence level is $\Gamma_{\text{eff}} > 1.3$.

The stacked 3–8 keV counts should have negligible contribution from host-galaxy X-ray emission; the contribution is only $\approx 3\%$ for host galaxies with a high X-ray luminosity of 10^{42} erg s $^{-1}$, which corresponds to a star-formation rate of $\approx 620 M_{\odot}$ yr $^{-1}$ (e.g., Lehmer et al. 2010). Therefore, the stacked signals are dominated by the nuclear sources. The soft stacked effective photon indices for the full sample ($1.8^{+0.5}_{-0.4}$) and the detected subsample ($1.5^{+0.4}_{-0.4}$) suggest that the targets on average are not absorbed by Compton-thick material, which would generally result in a flat ($\Gamma_{\text{eff}} \approx 0.5$ with a range of ≈ 0 –1) spectrum from 3–24 keV. Moreover, the soft stacked signal for the full sample cannot be dominated by one single object given their individual count contributions in the 3–8 keV band (three sources are not detected and the other three are weakly detected), indicating that at least two objects are responsible for the soft stacked Γ_{eff} . Therefore, at least 33% of the sample objects likely have soft effective photon indices ($\Gamma_{\text{eff}} \gtrsim 1.8$) and are likely not Compton-thick.

We also jointly fitted the *NuSTAR* spectra of the three detected targets, PG 0946, PG 1001, and PG 1254, with XSPEC v.12.8.1g (Arnaud 1996). We used the NUPRODUCTS script of NuSTARDAS to extract source spectra within the same $35''$ -radius circular apertures as in the photometry extraction, and local background spectra within annular regions with inner and outer radii of $120''$ and $240''$, respectively. The 3–24 keV spectra for the three targets in both FPMA and FPMB were fitted jointly with a simple power-law model using the C statistic (cstat) in XSPEC,²⁸ allowing each target to have its own redshift and Galactic column density. The best-fit photon index is $\Gamma = 1.55^{+0.30}_{-0.29}$ ($C = 290$ for 335 degrees of freedom), consistent with the stacked effective photon index for this subsample. The limited photon statistics of the spectra do not allow

²⁸ The W statistic was actually used in the presence of background spectra; see <http://heasarc.gsfc.nasa.gov/docs/xanadu/xspec/manual/XSappendixStatistics.html>.

for any useful constraint on Fe K α line emission at rest-frame 6.4–6.97 keV; a strong Fe K α line with an equivalent width of order 1–2 keV might be expected if the continuum is reflection dominated (e.g., Ghisellini et al. 1994; Matt et al. 1996; Gandhi et al. 2014). Previous *Chandra* or *XMM-Newton* observations do not provide useful constraints on the Fe K α line either (e.g., Imanishi & Terashima 2004).

4.2. Indirect Absorption Column-Density Constraints

We adopted the same approach described in Section 4.1.1 of L13 to constrain the absorption column densities indirectly for the six targets, under the assumption that the observed hard X-ray weakness is attributed entirely to absorption and they have nominal underlying X-ray emission as determined from the $\alpha_{\text{OX}}-L_{2500 \text{ \AA}}$ relation. Briefly, an absorption column density was derived by comparing the observed flux to the expected one derived from the expected α_{OX} assuming a power-law X-ray spectrum with $\Gamma = 1.8$. The MYTORUS XSPEC model, including both the transmitted and scattered spectral components, was used to calibrate the relation between N_{H} and this X-ray weakness.²⁹ We assumed a half-opening angle of 60° (corresponding to a torus covering factor of 0.5) and an inclination angle of 80° in the MYTORUS model. The N_{H} dependence on the assumed half-opening angle is relatively small, as illustrated in Figures 7 and 8 of L13 ($\approx 20\%$ smaller for a half-opening angle of 37°). Large inclination angles are generally expected for BAL quasars in the disk-wind scenario; for inclination angles smaller than 80° , we would derive larger N_{H} values by factors of up to ≈ 3 (Figures 7 and 8 of L13).

We derived column-density constraints using the 3–24 keV, 3–8 keV, and 8–24 keV *NuSTAR* fluxes or flux upper limits. The constraints in the 3–24 keV and 8–24 keV bands are comparable, and they are significantly tighter than those in the softer 3–8 keV band, as one would expect given the higher rest-frame energies utilized (also see Figures 7 and 8 of L13). We list in Table 2 the factors of 3–24 keV weakness and the 3–24 keV N_{H} constraints. The N_{H} uncertainty accounts for the measured flux uncertainty and the spread of the intrinsic α_{OX} value which was assumed to follow a Gaussian distribution with its 1σ uncertainty from Table 5 of Steffen et al. (2006). For the undetected targets, the lower limits on N_{H} were obtained from N_{H} probability distributions that were derived from the α_{OX} Gaussian distributions and the probability distributions of the 3–24 keV fluxes.³⁰ The column density constraints indicate that Compton-thick absorption is required for all six targets to produce the observed hard X-ray weakness if they have nominal intrinsic X-ray emission, as expected from our experimental design.

We note that these column density constraints were derived from the observed hard X-ray weakness, independent of the spectral-shape constraints above. In fact, Compton-thick absorption is likely inconsistent with a soft Γ_{eff} , as discussed in more detail below (Section 5.2).

5. DISCUSSION

²⁹ The physical properties of the shielding gas in BAL quasars are poorly understood (e.g., Proga & Kallman 2004). The parameterization of the MYTORUS model cannot fully reproduce the complex absorption environments of our targets, but we consider it the best available approximation for the purpose of deriving basic column-density constraints.

³⁰ The probability distributions of the 3–24 keV fluxes are from the probability distributions of the 3–24 keV counts, which were derived during our computation of the band ratios using the BEHR code.

5.1. Multiwavelength Properties

As in L13, we constructed infrared (IR) to X-ray spectral energy distributions (SEDs) for the targets, using photometric data from the *Wide-field Infrared Survey Explorer* (WISE; Wright et al. 2010), Two Micron All Sky Survey (2MASS; Skrutskie et al. 2006), SDSS, and/or *Galaxy Evolution Explorer* (GALEX; Martin et al. 2005) catalogs. The rest-frame SEDs are shown in Figure 3. The optical and UV data have been corrected for Galactic extinction following the dereddening approach of Cardelli et al. (1989) and O’Donnell (1994). Besides the strong intrinsic reddening in IRAS 07598 and IRAS 14026 (also see Jiang et al. 2013 for the reddening in IRAS 14026) and the significant X-ray weakness, these targets have typical radio-quiet quasar SEDs (e.g., Richards et al. 2006), similar to PG 1700 in the pilot sample.

Depending upon whether there are BALs from ions at low-ionization states such as Mg II or Al III, BAL quasars are classified as low-ionization BAL (LoBAL) or high-ionization BAL (HiBAL) quasars (e.g., Weymann et al. 1991; Sprayberry & Foltz 1992). LoBAL quasars constitute a minority ($\approx 10\%$) of BAL quasars, and they often show signs of dust reddening and are X-ray weaker than HiBAL quasars (e.g., Green et al. 2001; Gallagher et al. 2006; Gibson et al. 2009). Among our six targets here, IRAS 07598 and IRAS 14026 are LoBAL quasars (e.g., Hines & Wills 1995; Hines et al. 2001), while the other objects are HiBAL quasars (e.g., Turnshek et al. 1994; Arav et al. 2001). The two LoBAL quasars indeed show significant dust reddening and soft and hard X-ray weakness (Figure 3 and Table 2).

It has been suggested that significant X-ray weakness may be associated with super-Eddington accretion (e.g., Lusso et al. 2010). PG 1004 and PG 1700 in the pilot sample appear to have sub-Eddington accretion (Eddington ratios ≈ 0.09 and ≈ 0.41 ; L13), while Mrk 231 indeed appears to be a super-Eddington source with an Eddington ratio of ≈ 5 (Teng et al. 2014). We estimated bolometric luminosities for our targets from the Richards et al. (2006) composite quasar SED normalized to their 3000 Å luminosities (not strongly affected by intrinsic reddening), and collected their single-epoch virial black hole (BH) masses from the literature (Hao et al. 2005; Shen et al. 2011). These data are listed in Table 1. The derived Eddington ratios are in the range of 0.13 to 0.62, all in the sub-Eddington regime. However, there are significant uncertainties associated with the estimated BH masses (> 0.3 dex; e.g., Shen & Liu 2012) and bolometric luminosities, and thus it is difficult to assess whether the significant X-ray weakness is related to super-Eddington accretion in these cases.

The intrinsically X-ray weak quasar PHL 1811 has unusually weak and blueshifted high-ionization lines (e.g., the equivalent width of its C IV $\lambda 1549$ emission line is 6.6 Å, much smaller than the average value of ≈ 30 Å for SDSS quasars; Leighly et al. 2007a), which may be due to the lack of high-energy ionizing continuum photons. A recent study of IRAS 14026 (Jiang et al. 2013) suggests that it is probably a PHL 1811 analog given the weak C IV and C III] line emission, although no quantitative measurement of the line strength has been given. Wu et al. (2011) proposed a simple unification model (e.g., Figure 9 of Wu et al. 2011) where PHL 1811 analogs and BAL quasars have similar inner structures but the lines of sight to PHL 1811 analogs do not intercept the UV-absorbing disk wind. Confirmation of such a connection would facilitate our understanding of the nature of

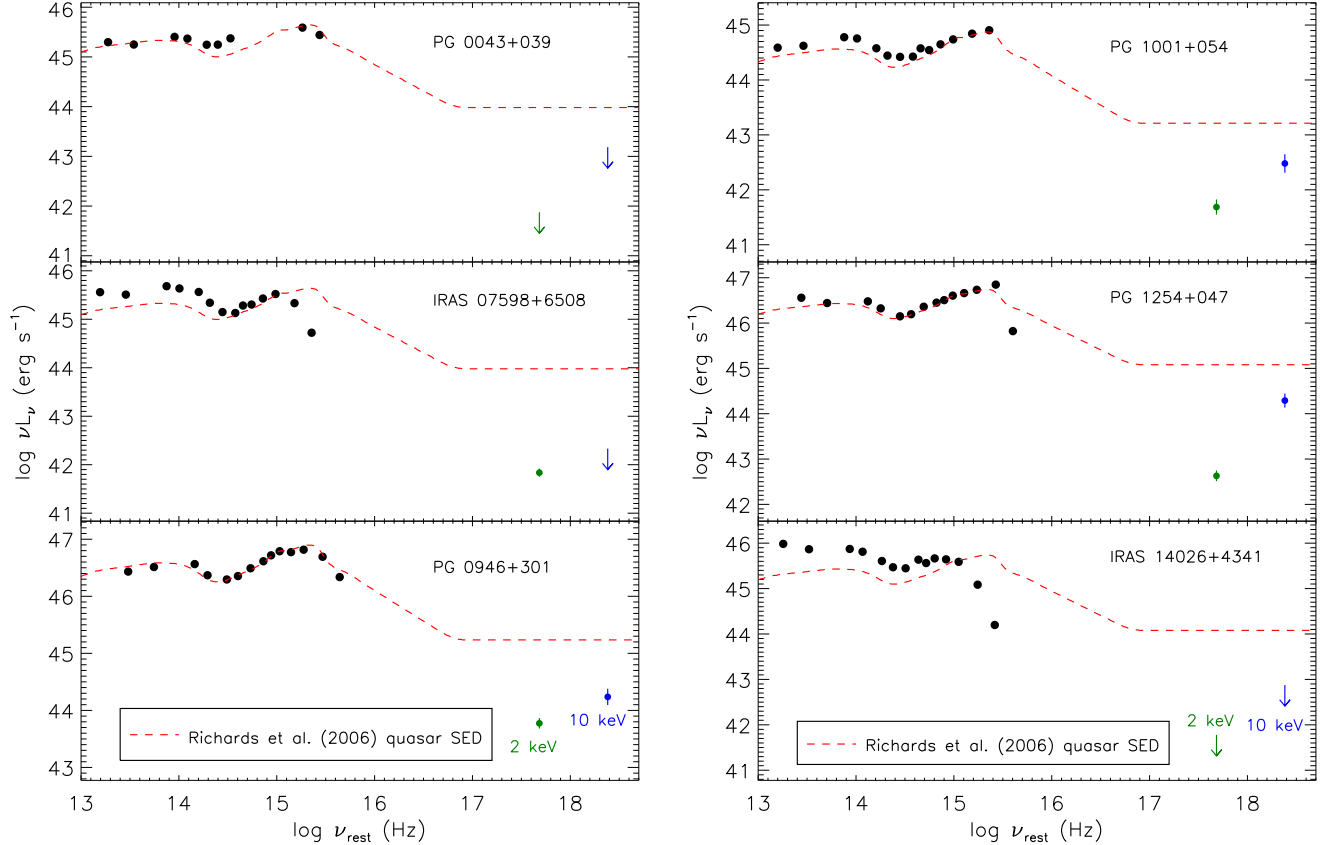


Figure 3. IR through X-ray SEDs of the six targets in the rest frame. The IR–UV data (black points) are from the *WISE*, *2MASS*, *SDSS*, and/or *GALEX* catalogs. The 2 keV data (green points and arrows) are from previous *Chandra* or *XMM-Newton* observations; note that IRAS 14026 was detected in the 2–8 keV band by *Chandra*, but not in the 0.5–2 keV band. The 10 keV data (blue points and arrows) were derived from the *NuSTAR* 3–24 keV fluxes or flux upper limits averaged over FPMA and FPMB assuming $\Gamma_{\text{eff}} = 1.2$ for PG 0946 and $\Gamma_{\text{eff}} = 1.8$ for the rest of the objects. The error bars for most of the data points are smaller than or comparable to the symbol size and are thus not visible. The SED data were not observed simultaneously and may be affected by variability (e.g., see the X-ray variability in Section 3). The red dashed curve shows the composite quasar SED of Richards et al. (2006) normalized to the 3000 Å luminosity.

their X-ray weakness. We visually examined the UV spectra for the other targets, the pilot sample, and also Mrk 231 (e.g., Hines & Wills 1995; Hamann 1998; Arav et al. 1999; Brandt et al. 2000; Gallagher et al. 2002b). The C IV emission lines appear strong in IRAS 07598, PG 0946, PG 1001, PG 1254, and Mrk 231, while they are either weak or are contaminated by the broad absorption features in PG 0043, PG 1004, and PG 1700. Therefore, more than half of our targets do not show weak C IV line emission as in PHL 1811. It is possible that intrinsically X-ray weak quasars may exhibit normal optical–UV emission lines if the accretion still produces sufficient EUV (perhaps $\lesssim 0.5$ keV) radiation to ionize the broad line regions, e.g., photons with energies exceeding 48 eV are required to ionize C III and produce the C IV emission line. A connection between BAL quasars and PHL 1811 analogs thus cannot be excluded.

5.2. Intrinsic X-ray Weakness in the Sample

As discussed extensively in L13, the hard X-ray weakness of these BAL quasars observed by *NuSTAR* can, in principle, be explained in either the Compton-thick absorption or intrinsic X-ray weakness scenarios. Without high photon counts, it is not feasible to constrain their nature individually via spectral analyses as was done for the case of the local object

Mrk 231. However, we have already established that there is apparently a population of intrinsically X-ray weak BAL quasars (L13; Teng et al. 2014), and we present below some evidence that at least some of our targets here are also intrinsically X-ray weak:

1. The soft stacked effective photon index ($1.8^{+0.5}_{-0.4}$) for the sample (Section 4.1) argues against Compton-thick absorption in general.³¹ This is similar to the independent *Chandra* stacking results in L13 where we also found a relatively soft stacked signal for a subsample of high-redshift BAL quasars, which suggests that the stacked source is not Compton-thick but is intrinsically X-ray weak. A soft 3–24 keV effective photon index is also consistent with the lower energy *Chandra* or *XMM-Newton* spectral fitting results (based on ≈ 45 –320 X-ray photons) for IRAS 07598, PG 0946, PG 1001, and PG 1254 where no or only moderate ($\lesssim 10^{23}$ cm^{−2}) absorption was found (e.g.,

³¹ For the two targets in L13, PG 1004 has a soft effective photon index (1.8 ± 0.5) but it could be dominated by jet emission, and PG 1700 has a hard effective photon index but with a large uncertainty (0.5 ± 0.7). The nature of their hard X-ray weakness is not clear.

Sabra & Hamann 2001; Imanishi & Terashima 2004; Schartel et al. 2005; Saez et al. 2012).³²

2. All six targets here and the two in the L13 pilot sample are significantly X-ray weak in the *NuSTAR* bands, which requires Compton-thick obscuration in the absorption scenario. If these BAL quasars with significant X-ray weakness represent an extension of the normal BAL-quasar population to higher column densities of $10^{23.5}-10^{25} \text{ cm}^{-2}$, then a first order expectation would be that they might consist of both Compton-thin and Compton-thick objects, similar to the overall AGN population. In this case, the chance of observing a sample of eight objects that are 100% Compton-thick is likely small. A natural explanation is that this is not a pure Compton-thick sample and at least some of the targets are intrinsically X-ray weak.

In Figure 4, we show the N_{H} distributions for our *NuSTAR* BAL-quasar sample (eight objects in total)³³ and those BAL quasars collected from the literature (Gallagher et al. 2002a; Giustini et al. 2008; Fan et al. 2009; Streblyanska et al. 2010; Morabito et al. 2014).³⁴ The combined distribution appears disjoint and perhaps bimodal, missing objects that are heavily obscured but Compton-thin, while the *NuSTAR* sample stands out in the Compton-thick regime forming an apparently distinct peak. The N_{H} distribution for typical low-redshift AGNs does not show such a bimodality (e.g., Figure 4 of Ueda et al. 2014). There is no obvious reason why BAL quasars would avoid the $N_{\text{H}} \approx (5-20) \times 10^{23} \text{ cm}^{-2}$ regime yet not higher N_{H} values, although we caution that our *NuSTAR* sample size is still relatively small and the apparent bimodality might be caused by small number statistics (moreover, we note that the shielding gas responsible for the X-ray absorption in BAL quasars is different from the dusty torus in typical obscured AGNs, and its nature is poorly understood). Thus, as a complement to the spectral-shape argument above, Figure 4 provides suggestive additional evidence that some of the *NuSTAR* objects are not absorbed by Compton-thick material but are intrinsically X-ray weak.

In obscured AGNs, there could be an additional soft X-ray continuum component arising from electron scattering of the intrinsic continuum in an ionized medium surrounding the central engine on a larger scale than the X-ray absorber. The scattering zone has a very small column density so that the scattered continuum has approximately the same shape as the intrinsic continuum.³⁵ Because of this, the scattered fraction is expected to be small, usually a few percent ($\approx 5\%$) or less (e.g., Turner et al. 1997; Ogle et al. 1999; Ueda et al.

2007; Young et al. 2007 and references therein). In principle, this ionized scattered component could perhaps dominate over the Compton-reflected component in the observed 3–24 keV emission of a Compton-thick AGN if the column density is sufficiently high ($N_{\text{H}} > 10^{25} \text{ cm}^{-2}$). In this case, the observed X-ray spectrum would appear soft and also be hard X-ray weak by a factor of ≈ 20 or more. This scenario could perhaps explain the soft stacked signal of our *NuSTAR* sample here without invoking intrinsic X-ray weakness. However, such a case would arguably be even more extraordinary than the discovery of intrinsically X-ray weak AGNs, as so far no compelling example of a clearly Compton-thick AGN with a soft $\approx 3-24$ keV continuum has been found (T. Yaqoob 2014, private communication). Furthermore, our X-ray variability detections for some objects (see Section 3) would constrain the size of any scattering medium. Therefore, we admit this possibility here but do not consider it likely.

Assuming that the observed hard X-ray weakness is entirely intrinsic with no absorption, these targets are intrinsically X-ray weak from 3–24 keV by the factors given in Table 2 (≈ 4 to > 25). If there is also absorption present that affects the observed 3–24 keV flux, similar to the case of Mrk 231, the factors of intrinsic X-ray weakness would be smaller. For comparison, Mrk 231 is intrinsically X-ray weak by a factor of ≈ 10 after the absorption correction (Teng et al. 2014), and PG 1004 and PG 1700 in L13 are X-ray weak by about the same factor in the intrinsic X-ray weakness scenario. The underlying physics responsible for intrinsic X-ray weakness is still unclear; some sort of coronal-quenching mechanism might be relevant for BAL quasars (Section 4.2.1 of L13 and references therein).

There are two LoBAL and four HiBAL quasars in our sample (Section 5.1). We checked the stacked signals for these two groups of sources separately. For LoBAL quasars (IRAS 07598 and IRAS 14026), the stacked source is only weakly detected in the 3–8 keV band, and the lower limit on the effective photon index is 1.0 (> 1.4 at a 1σ confidence level). For HiBAL quasars, the stacked effective photon index is $1.5^{+0.4}_{-0.4}$. Considering that the full sample has a soft effective photon index ($1.8^{+0.5}_{-0.4}$), the LoBAL quasars likely have soft photon indices. It thus appears likely that both groups contain intrinsically X-ray weak quasars.

All three detected targets show significant flux variability in the 3–8 keV band when compared to earlier observations (Section 3). Usually we would not expect such significant variability in a Compton-thick AGN where the 3–8 keV spectrum is likely dominated by a Compton-reflected component, as variability would be washed out during reflection over an extended region. However, for our BAL-quasar targets here, the X-ray absorber (shielding gas) is located on a significantly smaller physical scale than the torus in typical obscured AGNs ($\approx 10^{16}-10^{17} \text{ cm}$ vs. parsec scale) and the variability observed is on multi-year timescales. It is possible that a reflection-dominated spectrum could show long-term variability (e.g., Matt et al. 2004), and the scenario of Compton-thick absorption cannot be excluded by such variability. Due to the limited photon statistics of the *NuSTAR* and/or previous *Chandra* and *XMM-Newton* data, we cannot constrain the variability of the spectral shape (e.g., Γ_{eff}) for these three targets.

The fraction of intrinsically X-ray weak quasars among our sample objects is likely high. The soft stacked signal is not dominated by one single object, and a lower limit on the frac-

³² For the remaining two objects, PG 0043 is not detected by *XMM-Newton* and IRAS 14026 is weakly detected by *Chandra* and thus spectral analysis is not possible.

³³ The radio-loud nature of PG 1004 in L13 does not affect our analysis here. If its observed X-ray emission has a significant jet-linked contribution, the estimated N_{H} value would be larger (see Section 4.1.1 of L13).

³⁴ These are the X-ray studies of large samples of BAL quasars including N_{H} constraints in the literature. We caution that these data might not represent the real N_{H} distribution as the sample is not complete and the N_{H} constraints were obtained via different approaches.

³⁵ The location and physical properties of the scattering medium in BAL quasars are uncertain. The shielding gas itself might produce a relatively soft scattered continuum if it is sufficiently highly ionized (e.g., Proga & Kallman 2004; Ross & Fabian 2005; García & Kallman 2010).

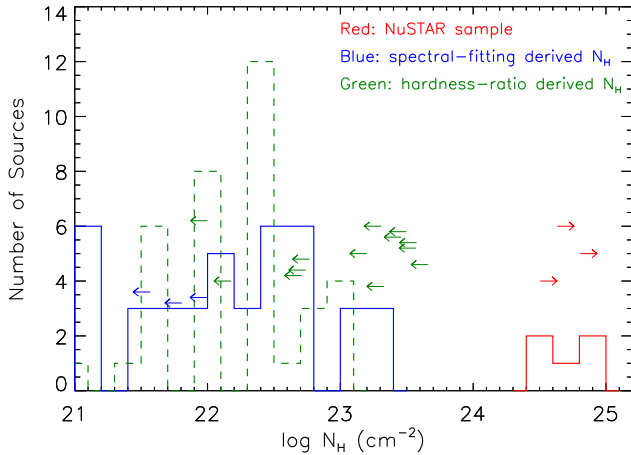


Figure 4. Distribution of the N_H constraints for the *NuSTAR* BAL-quasar sample (red histogram and lower limits), assuming the observed hard X-ray weakness is caused by absorption. For comparison, N_H distributions for typical BAL quasars collected from the literature (Gallagher et al. 2002a; Giustini et al. 2008; Fan et al. 2009; Streblyanska et al. 2010; Morabito et al. 2014) are shown as the blue (N_H derived from spectral fitting) and green (N_H derived from hardness-ratio analysis) histograms and upper limits. Sources with $N_H < 10^{21} \text{ cm}^{-2}$ are included in the $N_H = 10^{21} \text{ cm}^{-2}$ bin.

tion is 33% (at least two out of six being intrinsically X-ray weak) with an upper limit of 100% (all being intrinsically X-ray weak). Our targets were selected to be significantly X-ray weak in the $< 10 \text{ keV}$ band, and thus the intrinsic X-ray weakness fraction among the general BAL-quasar population will be lower. The fraction is estimated to be $\approx 17\text{--}40\%$ in the LBQS BAL-quasar sample (L13), much larger than the $\lesssim 2\%$ fraction among non-BAL quasars (Gibson et al. 2008). L13 suggested that the disk wind in an intrinsically X-ray weak quasar might have a large covering factor as it is likely easier to launch the wind when the nuclear X-ray emission is weak.³⁶ Thus intrinsically X-ray weak quasars would be preferentially observed as BAL quasars.

6. SUMMARY AND FUTURE WORK

We have presented *NuSTAR* observations of an extended sample of six BAL quasars with significant X-ray weakness in the $< 10 \text{ keV}$ band. All targets are either marginally or not detected by *NuSTAR*, indicating significant hard X-ray (8–24 keV) weakness as well, similar to the pilot sample in L13. The derived column-density constraints in an absorption scenario are all in the Compton-thick regime. However, stacking and joint spectral analyses of the data indicate a soft effective photon index, generally disfavoring Compton-thick absorption. Moreover, the uniform hard X-ray weakness observed in this sample and also the pilot sample suggests that the X-ray weakness is intrinsic in at least some of the targets. We conclude that *NuSTAR* observations of BAL-quasar samples have likely discovered a significant population ($\gtrsim 33\%$) of intrinsically X-ray weak sources among the BAL quasars with significantly weak $< 10 \text{ keV}$ emission. We emphasize that the disk wind in an intrinsically X-ray weak quasar might have a large covering factor, and thus the source would be preferentially observed as an BAL quasar.

It would be worthwhile to obtain additional *NuSTAR* observations of our targets, so that better constraints can be derived on the spectral shapes of individual and stacked sources. For

example, by tripling the exposure times, the three undetected sources should in general be detected in the 3–8 keV band and the stacked source of these three will probably be detected in the 8–24 keV band, as suggested by the current stacking results. Meanwhile, PG 1001 and PG 1254 should likely be individually detected in the 8–24 keV band. The improved spectral-shape constraints would provide a tighter constraint on the fraction of intrinsically X-ray weak quasars among this sample. Moreover, by increasing the exposure times by factors of $\approx 5\text{--}10$, sufficient photon statistics could probably be obtained for some individual targets to allow identification of intrinsically X-ray weak quasars in the sample via basic spectral analysis and accurate measurements of a soft Γ_{eff} . Such longer observations could be divided into a few segments to probe any short-term variability of the targets; ideally these segments should be separated by somewhat less than the expected light-crossing time of the shielding gas ($\approx 4\text{--}40$ days in the rest frame).

It would also be valuable to select additional intrinsically X-ray weak candidates for *NuSTAR* observations, although sources satisfying the selection criteria in Section 2 are rare largely due to the lack of systematic BAL-quasar selection at low redshifts ($z \lesssim 1.4$), where the key C IV transition is generally not accessible via ground-based spectroscopy. Such studies could probably also be extended to include “mini-BAL” quasars, which have narrower absorption troughs (500–2000 km s^{-1} wide) than BAL quasars yet may share their other properties (e.g., Trump et al. 2006).

Presently, the fraction of BAL quasars that are intrinsically X-ray weak is poorly constrained in the LBQS sample ($\approx 17\text{--}40\%$; L13), which was derived via stacking analysis of a sample of *Chandra* 2–8 keV undetected objects. We have scheduled additional 9–12 ks *Chandra* observations of the six undetected HiBAL quasars in the sample. Based on our current *Chandra* stacking results, we suspect that these observations will convert most of these non-detections into detections. This will set a much tighter and more robust upper limit upon the fraction of HiBAL quasars that are intrinsically X-ray weak. Further X-ray observations of the undetected LoBAL quasars in the sample may be pursued in future work. Such studies will benefit our assessment of the different fractions of intrinsically X-ray weak objects among BAL and non-BAL quasars.

We acknowledge support from the California Institute of Technology (Caltech) *NuSTAR* subcontract 44A-1092750 (BL, WNB), NASA ADP grant NNX10AC99G (BL, WNB), NASA Postdoctoral Program (SHT), CONICYT-Chile FONDECYT 1140304 (PA) and 1141218 (FEB), “EMBIGGEN” Anillo ACT1101 (PA, FEB), Basal-CATA PFB-06/2007 (FEB), Project IC120009 “Millennium Institute of Astrophysics (MAS)” of Iniciativa Científica Milenio del Ministerio de Economía, Fomento y Turismo (FEB), ASI/INAF grant I/037/12/0-011/13 (AC), STFC grant ST/J003697/1 (PG), and the Swiss National Science Foundation (NSF) grant PP00P2 138979/1 (MK). We thank K. Forster for help with the observation planning, and we thank T. Yaqoob for helpful discussions. We thank the referee for carefully reviewing the manuscript and providing helpful comments.

This work was supported under NASA Contract No. NNG08FD60C, and made use of data from the *NuSTAR* mis-

³⁶ Intrinsic X-ray weakness might also be associated with powerful large-scale outflows as suggested by Teng et al. (2014).

sion, a project led by Caltech, managed by the Jet Propulsion Laboratory, and funded by the National Aeronautics and Space Administration. We thank the *NuSTAR* Operations, Software and Calibration teams for support with the execution and analysis of these observations. This research has made use of NuSTARDAS jointly developed by the ASI Science Data Center (ASDC, Italy) and Caltech (USA).

REFERENCES

- Alexander, D. M., Stern, D., Del Moro, A., et al. 2013, *ApJ*, 773, 125
- Allen, J. T., Hewett, P. C., Maddox, N., Richards, G. T., & Belokurov, V. 2011, *MNRAS*, 410, 860
- Arav, N., de Kool, M., Korista, K. T., et al. 2001, *ApJ*, 561, 118
- Arav, N., Korista, K. T., de Kool, M., et al. 1999, *ApJ*, 516, 27
- Arnaud, K. A. 1996, in *ASP Conf. Ser.*, Vol. 101, *Astronomical Data Analysis Software and Systems V*, ed. G. H. Jacoby & J. Barnes, 17
- Ballo, L., Piconcelli, E., Schartel, N., & Vignali, C. 2008, *arXiv:0807.2225*
- Baumgartner, W. H., Tueller, J., Markwardt, C. B., et al. 2013, *ApJS*, 207, 19
- Becker, R. H., White, R. L., & Helfand, D. J. 1995, *ApJ*, 450, 559
- Brandt, W. N., Laor, A., & Wills, B. J. 2000, *ApJ*, 528, 637
- Cardelli, J. A., Clayton, G. C., & Mathis, J. S. 1989, *ApJ*, 345, 245
- Comastri, A., Ranalli, P., Iwasawa, K., et al. 2011, *A&A*, 526, L9
- Condon, J. J., Cotton, W. D., Greisen, E. W., et al. 1998, *AJ*, 115, 1693
- Dickey, J. M., & Lockman, F. J. 1990, *ARA&A*, 28, 215
- Fan, L. L., Wang, H. Y., Wang, T., et al. 2009, *ApJ*, 690, 1006
- Freeman, P. E., Kashyap, V., Rosner, R., & Lamb, D. Q. 2002, *ApJS*, 138, 185
- Gallagher, S. C., Brandt, W. N., Chartas, G., & Garmire, G. P. 2002a, *ApJ*, 567, 37
- Gallagher, S. C., Brandt, W. N., Chartas, G., Garmire, G. P., & Sambruna, R. M. 2002b, *ApJ*, 569, 655
- Gallagher, S. C., Brandt, W. N., Chartas, G., et al. 2006, *ApJ*, 644, 709
- Gallagher, S. C., Brandt, W. N., Laor, A., et al. 2001, *ApJ*, 546, 795
- Gallagher, S. C., Brandt, W. N., Sambruna, R. M., Mathur, S., & Yamasaki, N. 1999, *ApJ*, 519, 549
- Gallagher, S. C., Brandt, W. N., Wills, B. J., et al. 2004, *ApJ*, 603, 425
- Gandhi, P., Lansbury, G. B., Alexander, D. M., et al. 2014, *ApJ*, in press (*arXiv:1407.1844*)
- García, J., & Kallman, T. R. 2010, *ApJ*, 718, 695
- Gehrels, N. 1986, *ApJ*, 303, 336
- George, I. M., & Fabian, A. C. 1991, *MNRAS*, 249, 352
- Ghisellini, G., Haardt, F., & Matt, G. 1994, *MNRAS*, 267, 743
- Gibson, R. R., & Brandt, W. N. 2012, *ApJ*, 746, 54
- Gibson, R. R., Brandt, W. N., & Schneider, D. P. 2008, *ApJ*, 685, 773
- Gibson, R. R., Jiang, L., Brandt, W. N., et al. 2009, *ApJ*, 692, 758
- Giustini, M., Cappi, M., & Vignali, C. 2008, *A&A*, 491, 425
- Green, P. J., Aldcroft, T. L., Mathur, S., Wilkes, B. J., & Elvis, M. 2001, *ApJ*, 558, 109
- Haardt, F., & Maraschi, L. 1991, *ApJ*, 380, L51
- Hamann, F. 1998, *ApJ*, 500, 798
- Hao, C. N., Xia, X. Y., Mao, S., Wu, H., & Deng, Z. G. 2005, *ApJ*, 625, 78
- Harrison, F. A., Craig, W. W., Christensen, F. E., et al. 2013, *ApJ*, 770, 103
- Hewett, P. C., & Foltz, C. B. 2003, *AJ*, 125, 1784
- Hines, D. C., Schmidt, G. D., Gordon, K. D., et al. 2001, *ApJ*, 563, 512
- Hines, D. C., & Wills, B. J. 1995, *ApJ*, 448, L69
- Imanishi, M., & Terashima, Y. 2004, *AJ*, 127, 758
- Jiang, P., Zhou, H., Ji, T., et al. 2013, *AJ*, 145, 157
- Just, D. W., Brandt, W. N., Shemmer, O., et al. 2007, *ApJ*, 665, 1004
- Kellermann, K. I., Sramek, R., Schmidt, M., Shaffer, D. B., & Green, R. 1989, *AJ*, 98, 1195
- Komatsu, E., Smith, K. M., Dunkley, J., et al. 2011, *ApJS*, 192, 18
- Kraft, R. P., Burrows, D. N., & Nousek, J. A. 1991, *ApJ*, 374, 344
- Lansbury, G. B., Alexander, D. M., Del Moro, A., et al. 2014, *ApJ*, 785, 17
- Lehmer, B. D., Alexander, D. M., Bauer, F. E., et al. 2010, *ApJ*, 724, 559
- Leighly, K. M., Halpern, J. P., Jenkins, E. B., & Casebeer, D. 2007a, *ApJS*, 173, 1
- Leighly, K. M., Halpern, J. P., Jenkins, E. B., et al. 2007b, *ApJ*, 663, 103
- Luo, B., Brandt, W. N., Alexander, D. M., et al. 2013, *ApJ*, 772, 153 (L13)
- Lusso, E., Comastri, A., Vignali, C., et al. 2010, *A&A*, 512, A34
- Martin, D. C., Fanson, J., Schiminovich, D., et al. 2005, *ApJ*, 619, L1
- Mathur, S., Green, P. J., Arav, N., et al. 2000, *ApJ*, 533, L79
- Matt, G., Bianchi, S., Guainazzi, M., & Molendi, S. 2004, *A&A*, 414, 155
- Matt, G., Brandt, W. N., & Fabian, A. C. 1996, *MNRAS*, 280, 823
- Miller, B. P., Brandt, W. N., Gallagher, S. C., et al. 2006, *ApJ*, 652, 163
- Miller, B. P., Brandt, W. N., Schneider, D. P., et al. 2011, *ApJ*, 726, 20
- Morabito, L. K., Dai, X., Leighly, K. M., Sivakoff, G. R., & Shankar, F. 2014, *ApJ*, 786, 58
- Murphy, K. D., & Yaqoob, T. 2009, *MNRAS*, 397, 1549
- Murray, N., Chiang, J., Grossman, S. A., & Voit, G. M. 1995, *ApJ*, 451, 498
- O'Donnell, J. E. 1994, *ApJ*, 422, 158
- Ogle, P. M., Cohen, M. H., Miller, J. S., et al. 1999, *ApJS*, 125, 1
- Park, T., Kashyap, V. L., Siemiginowska, A., et al. 2006, *ApJ*, 652, 610
- Proga, D., & Kallman, T. R. 2004, *ApJ*, 616, 688
- Proga, D., Stone, J. M., & Kallman, T. R. 2000, *ApJ*, 543, 686
- Richards, G. T., Lacy, M., Storrie-Lombardi, L. J., et al. 2006, *ApJS*, 166, 470
- Ross, R. R., & Fabian, A. C. 2005, *MNRAS*, 358, 211
- Rovilos, E., Georgantopoulos, I., Akylas, A., et al. 2014, *MNRAS*, 438, 494
- Sabra, B. M., & Hamann, F. 2001, *ApJ*, 563, 555
- Saez, C., Brandt, W. N., Gallagher, S. C., Bauer, F. E., & Garmire, G. P. 2012, *ApJ*, 759, 42
- Schartel, N., Rodríguez-Pascual, P. M., Santos-Lleó, M., et al. 2005, *A&A*, 433, 455
- Schmidt, M., & Green, R. F. 1983, *ApJ*, 269, 352
- Schneider, D. P., Richards, G. T., Hall, P. B., et al. 2010, *AJ*, 139, 2360
- Shen, Y., & Liu, X. 2012, *ApJ*, 753, 125
- Shen, Y., Richards, G. T., Strauss, M. A., et al. 2011, *ApJS*, 194, 45
- Skrutskie, M. F., Cutri, R. M., Stiening, R., et al. 2006, *AJ*, 131, 1163
- Sprayberry, D., & Foltz, C. B. 1992, *ApJ*, 390, 39
- Steffen, A. T., Strateva, I., Brandt, W. N., et al. 2006, *AJ*, 131, 2826
- Streblyanska, A., Barcons, X., Carrera, F. J., & Gil-Merino, R. 2010, *A&A*, 515, A2
- Teng, S. H., Brandt, W. N., Harrison, F. A., et al. 2014, *ApJ*, 785, 19
- Trump, J. R., et al. 2006, *ApJS*, 165, 1
- Turner, T. J., George, I. M., Nandra, K., & Mushotzky, R. F. 1997, *ApJ*, 488, 164
- Turnshek, D. A., Espey, B. R., Kopko, Jr., M., et al. 1994, *ApJ*, 428, 93
- Ueda, Y., Akiyama, M., Hasinger, G., Miyaji, T., & Watson, M. G. 2014, *ApJ*, 786, 104
- Ueda, Y., Eguchi, S., Terashima, Y., et al. 2007, *ApJ*, 664, L79
- Vanden Berk, D. E., Richards, G. T., Bauer, A., et al. 2001, *AJ*, 122, 549
- Weymann, R. J., Morris, S. L., Foltz, C. B., & Hewett, P. C. 1991, *ApJ*, 373, 23
- Wik, D. R., Hornstrup, A., Molendi, S., et al. 2014, *ApJ*, submitted (*arXiv:1403.2722*)
- Wright, E. L., Eisenhardt, P. R. M., Mainzer, A. K., et al. 2010, *AJ*, 140, 1868
- Wu, J., Brandt, W. N., Hall, P. B., et al. 2011, *ApJ*, 736, 28
- York, D. G., Adelman, J., Anderson, Jr., J. E., et al. 2000, *AJ*, 120, 1579
- Young, S., Axon, D. J., Robinson, A., Hough, J. H., & Smith, J. E. 2007, *Nature*, 450, 74

Table 1
NuSTAR Observation Log and Target Properties

Object Name (1)	z (2)	m_B (3)	M_B (4)	Observation Start Date (5)	Observation ID (6)	Exp (ks) (7)	Exp_clean (ks) (8)	Δ_{OX} (arcsec) (9)	$\log M_{\text{BH}}$ (M_{\odot}) (10)	$\log L_{\text{bol}}$ (erg s^{-1}) (11)	BAL Type (12)
PG 0043+039	0.385	15.9	-25.5	2013 Jul 18	60001119002	21.5	20.2	...	9.0 ^a	46.2	HiBAL
IRAS 07598+6508	0.148	14.9	-24.3	2013 Oct 29	60001120002	30.2	28.1	...	8.3 ^a	46.2	LoBAL
PG 0946+301	1.223	16.0	-28.2	2013 Nov 09	60001124002	37.4	34.9	6.9	9.8 ^b	47.5	HiBAL
PG 1001+054	0.161	16.1	-23.2	2013 Jun 28	60001122002	20.9	19.6	8.0	7.7 ^b	45.5	HiBAL
PG 1254+047	1.026	15.8	-28.0	2013 Jun 27	60001123002	31.7	29.4	2.9	9.7 ^b	47.3	HiBAL
IRAS 14026+4341	0.323	15.7	-25.3	2013 Nov 10	60001121002	27.8	26.0	...	8.6 ^b	46.3	LoBAL

Note. — Cols. (1) and (2): object name and redshift. Cols. (3) and (4): apparent and absolute B -band magnitudes. Cols. (5) and (6): *NuSTAR* observation start date and observation ID. Cols. (7) and (8): nominal and cleaned *NuSTAR* exposure times, respectively. Col. (9): minimum positional offset between the optical and X-ray positions. The X-ray positions are determined from WAVDETECT detections in the 3–24 keV images of FPMA and FPMB. Blank entries indicate non-detections. Col. (10): virial BH mass from the literature; (a): Hao et al. (2005); (b): Shen et al. (2011). Col. (11): bolometric luminosity calculated from the scaled Richards et al. (2006) composite quasar SED. Col. (12): BAL quasar type depending upon whether there are BALs from ions at low-ionization states.

Table 2
NuSTAR Photometry and Column-Density Constraints

Object Name and FPM	Net Counts			$\Gamma_{\text{eff}}^{\text{a}}$	Flux ($10^{-14} \text{ erg cm}^{-2} \text{ s}^{-1}$)			$\log L$ (erg s^{-1})	$f_{\text{weak}}^{\text{b}}$	N_{H}^{c} (10^{24} cm^{-2})
	3–24 keV	3–8 keV	8–24 keV		3–24 keV	3–8 keV	8–24 keV			
PG 0043+039 A	< 21.8	< 17.2	< 12.7	1.8	< 7.2	< 3.9	< 6.2	< 43.6	> 7.3	> 2.8
PG 0043+039 B	< 18.1	< 11.6	< 15.3	1.8	< 6.4	< 2.8	< 8.1	< 43.5	> 8.4	> 3.2
IRAS 07598+6508 A	< 41.4	< 28.2	< 21.0	1.8	< 8.7	< 4.1	< 6.6	< 42.7	> 22.5	> 5.8
IRAS 07598+6508 B	< 34.2	< 27.8	< 16.9	1.8	< 7.6	< 4.2	< 5.6	< 42.6	> 24.7	> 6.4
PG 0946+301 A	44.6 ^{+15.2} _{-13.5}	21.9 ^{+10.9} _{-9.2}	22.7 ^{+11.6} _{-9.9}	1.2 ^{+0.9} _{-0.8}	8.7 ± 3.4	2.4 ± 1.1	6.2 ± 3.1	44.9 ± 0.1	3.4	2.1 ^{+3.6} _{-1.8}
PG 0946+301 B	36.4 ^{+16.0} _{-14.4}	< 35.5	< 36.8	1.8	6.4 ± 2.9	< 4.3	< 9.7	44.8 ± 0.2	4.6	3.0 ^{+5.0} _{-2.2}
PG 1001+054 A	25.0 ^{+11.3} _{-9.8}	17.5 ^{+9.0} _{-7.2}	< 20.3	> 0.4	8.5 ± 4.0	4.1 ± 1.9	< 10.2	42.8 ± 0.2	22.7	6.0 ^{+10.1} _{-3.6}
PG 1001+054 B	26.4 ^{+12.5} _{-10.8}	17.6 ^{+9.7} _{-8.0}	< 20.6	> 0.4	9.3 ± 4.6	4.2 ± 2.1	< 10.8	42.8 ± 0.2	20.4	5.4 ^{+10.0} _{-3.3}
PG 1254+047 A	30.6 ^{+13.8} _{-12.2}	< 27.3	< 33.2	1.8	6.8 ± 3.1	< 4.2	< 11.0	44.6 ± 0.2	5.7	3.4 ^{+6.1} _{-2.4}
PG 1254+047 B	39.0 ^{+15.7} _{-14.1}	27.0 ^{+12.0} _{-10.4}	< 31.0	> 0.4	9.2 ± 4.0	4.4 ± 1.8	< 11.0	44.7 ± 0.2	4.2	2.5 ^{+4.2} _{-1.9}
IRAS 14026+4341 A	< 20.7	< 15.5	< 13.7	1.8	< 4.7	< 2.4	< 4.7	< 43.2	> 12.5	> 4.3
IRAS 14026+4341 B	< 25.9	< 28.6	< 11.8	1.8	< 6.3	< 4.8	< 4.3	< 43.3	> 9.7	> 3.4

^a Effective photon index, derived based on the band ratio between the observed 8–24 keV and 3–8 keV counts, assuming a power-law model with Galactic absorption. $\Gamma_{\text{eff}} = 1.8$ is assumed if it cannot be constrained.

^b Factor of X-ray weakness in the 3–24 keV band, $f_{\text{weak}} = F_{\text{expected}}/F_{\text{observed}}$. The expected flux was derived based on the expected α_{OX} (from the $\alpha_{\text{OX}}-L_{2500 \text{ \AA}}$ relation) and a power-law X-ray spectrum with $\Gamma = 1.8$. The scatter of the expected flux was accounted for when deriving the lower limit for an undetected source.

^c Absorption column-density constraint derived from the factor of 3–24 keV weakness using the MYTORUS model.